INTERNATIONAL JOURNAL FOR NUMERICAL METHODS IN FLUIDS
Int. J. Numer. Meth. Fluids 2009; **60**:565–589
Published online 17 September 2008 in Wiley InterScience (www.interscience.wiley.com). DOI: 10.1002/fld.1905

PML absorbing boundary conditions for the linearized and nonlinear Euler equations in the case of oblique mean flow

Sarah A. Parrish and Fang Q. Hu*, †

Department of Mathematics and Statistics, Old Dominion University, Norfolk, VA, U.S.A.

SUMMARY

For the case of uniform mean flow in an arbitrary direction, perfectly matched layer (PML) absorbing boundary conditions are presented for both the linearized and nonlinear Euler equations. Although linear perfectly matched side layers with an oblique mean flow have been studied in previous works, we propose in the present paper a construction of corner layer equations that are dynamically stable. Stability issues are investigated by examining the dispersion relations of linear waves supported by the corner layer equations. For increased efficiency, a pseudo mean flow is included in the derivation of the PML equations for the nonlinear case. Numerical examples are given to support the validity of the proposed equations. Specifically, the linear PML formulation is tested for the case of acoustic, vorticity, and entropy waves traveling with an oblique mean flow. The nonlinear formulation is tested with an isentropic vortex moving diagonally with a constant velocity. Copyright © 2008 John Wiley & Sons, Ltd.

Received 27 November 2007; Revised 2 July 2008; Accepted 14 July 2008

KEY WORDS: perfectly matched layer; computational aeroacoustics; Euler equations; absorbing boundary conditions; nonreflecting boundary conditions; computational fluid dynamics

1. INTRODUCTION

The use of a nonreflecting boundary condition is imperative when considering aeroacoustic problems with an open physical domain, as reflections originating from the numerical boundaries can compromise the accuracy of the solution within the computational domain. Further, as the accuracy of spatial and temporal discretizations increases, the need for greater accuracy at the boundaries increases accordingly. The perfectly matched layer (PML) technique has proven effective in eliminating boundary reflections with sufficient accuracy, as was first proposed by Bérenger for Maxwell's equations [1]. However, most of the work done for PML in fluid dynamics has

*Correspondence to: Fang Q. Hu, Department of Mathematics and Statistics, Old Dominion University, Norfolk, VA, U.S.A.
†E-mail: fhu@odu.edu

Contract/grant sponsor: National Science Foundation; contract/grant number: DMS-0411402

Copyright © 2008 John Wiley & Sons, Ltd.

been specific to mean or background flow that is perpendicular to a boundary, as is the case, for example, in [2–7]. Previous works on the PML for oblique flows include [8–10]. In [8], the PML for a mean flow oblique to the Euler and PML interface was given. However, the equations for the corner layers were not derived. In [9], only the acoustic waves were considered for an oblique mean flow. In [10], a new formulation of PML for the linear Euler equations based on the Smith factorizations was given in which the direction of the mean flow can be arbitrary. However, whether this approach can be extended to nonlinear equations remains to be seen. The goal of this paper is to apply the PML technique to the more general case of mean flow in an arbitrary direction for both the linear and the nonlinear applications. Such a formulation can be useful in many practical applications, such as when an aircraft travels at a nonzero angle of attack, when a slant boundary is present, or when a transformed coordinate is used in the computation.

The challenge, when applying the PML technique to such a problem, lies in correcting the inconsistencies in the phase and group velocities [2, 4, 7, 11]. A simple space–time transformation has been shown necessary and effective in removing the inconsistency for acoustic waves alone [7], but when inconsistencies also arise in the group and phase velocities of the vorticity and entropy waves, as is the case when dealing with an oblique flow, no such transformation has been found. Our approach in this paper is to derive the side and corner layers independently. The side layers will be perfectly matched, while linear stability analysis will show the corner layers to be dynamically stable.

The next section examines the dispersion relations of linear waves supported by the Euler equations in the presence of an oblique mean flow. The derivations of the PML equations for the linearized and the nonlinear Euler equations are then presented, followed by an examination of the stability of the derived corner equations. Finally, numerical examples are given to show the effectiveness of the proposed equations.

2. DISPERSION RELATIONS OF LINEAR WAVES

To understand the challenge of forming PML equations for an oblique mean flow, consider the two-dimensional linearized Euler equations with components of mean flow (M_x, M_y)

$$\frac{\partial \mathbf{u}}{\partial t}+\mathbf{A}\frac{\partial \mathbf{u}}{\partial x}+\mathbf{B}\frac{\partial \mathbf{u}}{\partial y}=0 \tag{1a}$$

$$\mathbf{u}=\begin{pmatrix}\rho\\ u\\ v\\ p\end{pmatrix},\quad \mathbf{A}=\begin{pmatrix}M_x & 1 & 0 & 0\\ 0 & M_x & 0 & 1\\ 0 & 0 & M_x & 0\\ 0 & 1 & 0 & M_x\end{pmatrix},\quad \mathbf{B}=\begin{pmatrix}M_y & 0 & 1 & 0\\ 0 & M_y & 0 & 0\\ 0 & 0 & M_y & 1\\ 0 & 0 & 1 & M_y\end{pmatrix} \tag{1b}$$

where ρ is the density, u and v are velocity components, p is the pressure, and M_x and M_y are the Mach numbers in the x- and y-directions, respectively.

For linear waves, the dispersion relations for (1a) are known to be

$$(\omega-M_xk_x-M_yk_y)^2-k_x^2-k_y^2=0 \tag{2}$$

Copyright © 2008 John Wiley & Sons, Ltd.

DOI: 10.1002/fld

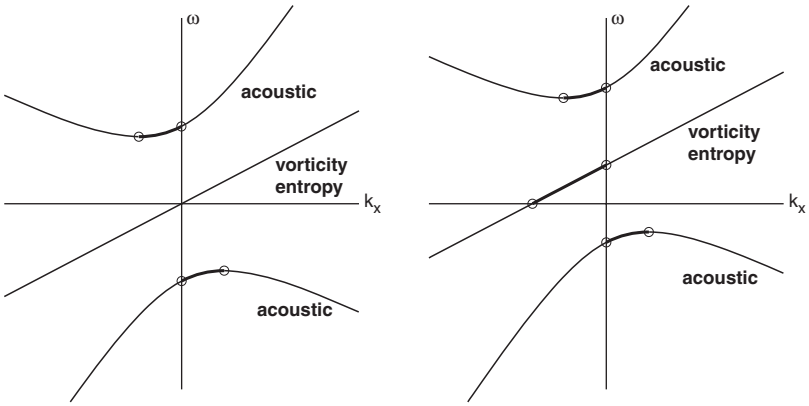

Figure 1. Dispersion relations of linear waves for $M_y = 0$ (left) and $M_y \neq 0$ (right).

for acoustic waves and

$$\omega - M_x k_x - M_y k_y = 0 \tag{3}$$

for vorticity and entropy waves. The left side of Figure 1 plots these relations for ω as a function of k_x for the case $M_y = 0$ and for a fixed k_y. In quadrants II and IV, where phase velocity is negative, segments of the curves for the acoustic waves have positive group velocity, which is not consistent with the negative phase velocity. These inconsistencies will lead to numerical instability if not corrected before the PML change of variables is applied in the derivation [2, 7]. Notice that because the inconsistencies only appear in the acoustic waves, a linear space–time transformation like those used in [7, 11–13] is sufficient to correct the problem. However, in the case of oblique flow, where M_y is nonzero, inconsistencies appear not only in the acoustic waves, but also in the vorticity and the entropy waves, as shown on the right of Figure 1. In such a case, no transformation has been found to remove the inconsistencies for all three types of waves.

An alternate approach is to derive the side and corner layers independently. Figure 2 illustrates the placement of proposed x-, y-, and corner layers for a truncated domain. In [8], where only x-layers are present, it is suggested that by replacing the time derivative with a material derivative involving M_y, the PML derived for $M_y = 0$ can still be used. Unfortunately, when both x- and y-layers are present, corner layers will inevitably exist, and while a moving-frame can be used to eliminate the part of the mean flow in the transverse direction, no such remedy can be used for the corner layers. In the present formulation, by deriving the x- and y-layers separately, corner layers will be formed as a combination of the x- and y-layers. The derivations are presented in the following sections.

3. PML FOR THE LINEARIZED EULER EQUATIONS WITH OBLIQUE MEAN FLOW

As mentioned above, PML equations for the x- and y-layers will be given first. Starting with the x-layer, we begin the derivation for the linearized Euler equations by applying a moving-frame

Copyright © 2008 John Wiley & Sons, Ltd.

DOI: 10.1002/fld

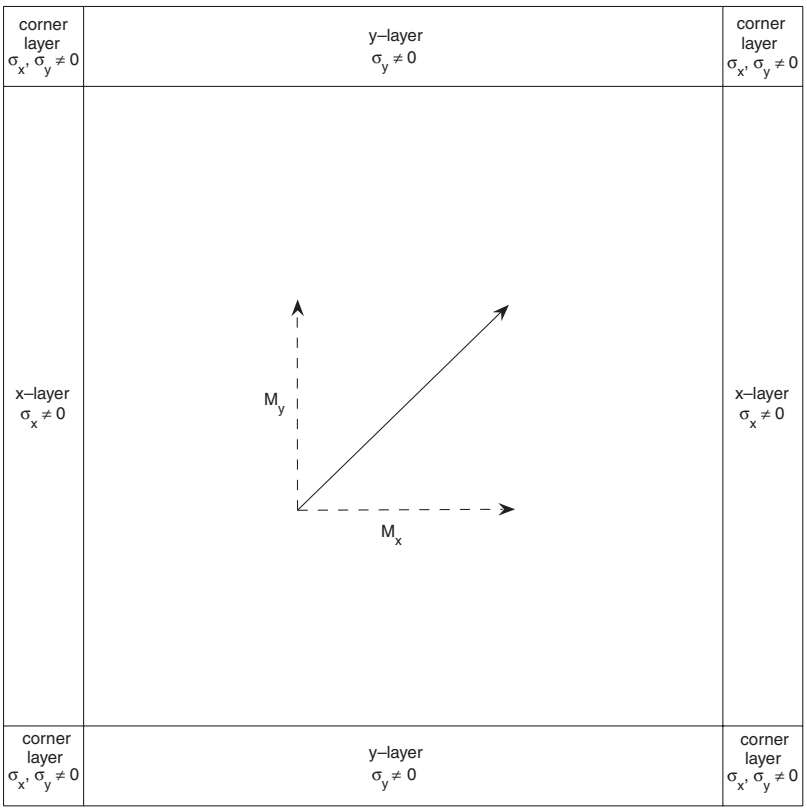

Figure 2. Separate layers for x and y allow us to effectively remove all inconsistencies in phase and group velocities.

change of variables

$$\hat{x} = x \tag{4a}$$

$$\hat{y} = y - M_y t \tag{4b}$$

$$\hat{t} = t \tag{4c}$$

that gives

$$\frac{\partial}{\partial x} = \frac{\partial}{\partial \hat{x}} \tag{5a}$$

$$\frac{\partial}{\partial y} = \frac{\partial}{\partial \hat{y}} \tag{5b}$$

$$\frac{\partial}{\partial t} = \frac{\partial}{\partial \hat{t}} - M_y \frac{\partial}{\partial \hat{y}} \tag{5c}$$

Copyright © 2008 John Wiley & Sons, Ltd.

DOI: 10.1002/fld

The linearized Euler equation (1a) then becomes

$$\frac{\partial \mathbf{u}}{\partial \hat{t}} - M_y \frac{\partial \mathbf{u}}{\partial \hat{y}} + \mathbf{A}\frac{\partial \mathbf{u}}{\partial \hat{x}} + \mathbf{B}\frac{\partial \mathbf{u}}{\partial \hat{y}} = 0 \tag{6}$$

or

$$\frac{\partial \mathbf{u}}{\partial \hat{t}} + \mathbf{A}\frac{\partial \mathbf{u}}{\partial \hat{x}} + \mathbf{B}_0\frac{\partial \mathbf{u}}{\partial \hat{y}} = 0 \tag{7}$$

where

$$\mathbf{B}_0 = \mathbf{B} - M_y \mathbf{I} \tag{8}$$

Equation (7) is equivalent to the case where $M_y = 0$. Therefore, the PML equations presented in [7] can be readily applied, giving

$$\frac{\partial \mathbf{u}}{\partial \hat{t}} + \mathbf{A}\frac{\partial \mathbf{u}}{\partial \hat{x}} + \mathbf{B}_0\frac{\partial \mathbf{u}}{\partial \hat{y}} + \sigma_x \mathbf{B}_0 \frac{\partial \mathbf{q}_1}{\partial \hat{y}} + \sigma_x \mathbf{u} + \sigma_x \beta_x \mathbf{A}\mathbf{u} = 0 \tag{9a}$$

$$\frac{\partial \mathbf{q}_1}{\partial \hat{t}} = \mathbf{u} \tag{9b}$$

where

$$\beta_x = \frac{M_x}{1 - M_x^2} \tag{10}$$

and σ_x is the absorption coefficient, which depends on x only. Reverting back to the original time and space coordinates, we obtain

$$\frac{\partial \mathbf{u}}{\partial t} + \mathbf{A}\frac{\partial \mathbf{u}}{\partial x} + \mathbf{B}\frac{\partial \mathbf{u}}{\partial y} + \sigma_x \mathbf{B}_0 \frac{\partial \mathbf{q}_1}{\partial y} + \sigma_x \mathbf{u} + \sigma_x \beta_x \mathbf{A}\mathbf{u} = 0 \tag{11a}$$

$$\frac{\partial \mathbf{q}_1}{\partial t} + M_y \frac{\partial \mathbf{q}_1}{\partial y} = \mathbf{u} \tag{11b}$$

Using a similar approach, we find the y-layer equations:

$$\frac{\partial \mathbf{u}}{\partial t} + \mathbf{A}\frac{\partial \mathbf{u}}{\partial x} + \mathbf{B}\frac{\partial \mathbf{u}}{\partial y} + \sigma_y \mathbf{A}_0 \frac{\partial \mathbf{q}_2}{\partial x} + \sigma_y \mathbf{u} + \sigma_y \beta_y \mathbf{B}\mathbf{u} = 0 \tag{12a}$$

$$\frac{\partial \mathbf{q}_2}{\partial t} + M_x \frac{\partial \mathbf{q}_2}{\partial x} = \mathbf{u} \tag{12b}$$

where

$$\mathbf{A}_0 = \mathbf{A} - M_x \mathbf{I} \tag{13}$$

and

$$\beta_y = \frac{M_y}{1 - M_y^2} \tag{14}$$

Copyright © 2008 John Wiley & Sons, Ltd.

DOI: 10.1002/fld

and σ_y is another absorption coefficient, which depends on y only. In the above, $\mathbf{q}_1$ and $\mathbf{q}_2$ are the auxiliary variables for x- and y-layers, respectively.

For equations to be used in the corner layers where both σ_x and σ_y are nonzero, we combine the x- and y-layer equations as follows:

$$\frac{\partial \mathbf{u}}{\partial t}+\mathbf{A}\frac{\partial \mathbf{u}}{\partial x}+\mathbf{B}\frac{\partial \mathbf{u}}{\partial y}+\sigma_y\mathbf{A}_0\frac{\partial \mathbf{q}_2}{\partial x}+\sigma_x\mathbf{B}_0\frac{\partial \mathbf{q}_1}{\partial y}+(\sigma_x+\sigma_y)\mathbf{u}+\sigma_x\beta_x\mathbf{A}\mathbf{u}+\sigma_y\beta_y\mathbf{B}\mathbf{u}=0 \tag{15a}$$

$$\frac{\partial \mathbf{q}_1}{\partial t}+M_y\frac{\partial \mathbf{q}_1}{\partial y}+\sigma_y\mathbf{q}_1=\mathbf{u} \tag{15b}$$

$$\frac{\partial \mathbf{q}_2}{\partial t}+M_x\frac{\partial \mathbf{q}_2}{\partial x}+\sigma_x\mathbf{q}_2=\mathbf{u} \tag{15c}$$

where the $\sigma_y\mathbf{q}_1$ and $\sigma_x\mathbf{q}_2$ terms, in (15b) and (15c), respectively, have been added for stability. Clearly, when σ_y or σ_x is zero, Equation set (15) reduces to the x- or y-layer equation sets, (11) or (12), respectively. Although other forms for the added terms are possible, we find the present version given in (15b) and (15c) simple and sufficient for stability. Although the side layers are perfectly matched to the interior Euler domain, the interfaces between the corner and side layers are no longer perfectly matched. However, as we will see later, the performance of the corner layer is numerically satisfactory. We will also show later that the corner layer equations are dynamically stable. A detailed stability analysis is presented in Section 5.

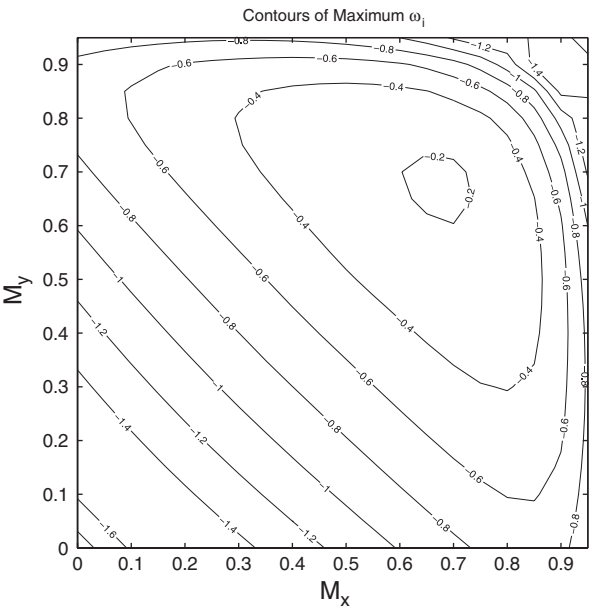

Figure 3. Contours of maximum imaginary part of ω for $\sigma_x=\sigma_y=2$ and $|k_x|, |k_y|\leqslant 20$.

Copyright © 2008 John Wiley & Sons, Ltd.

DOI: 10.1002/fld

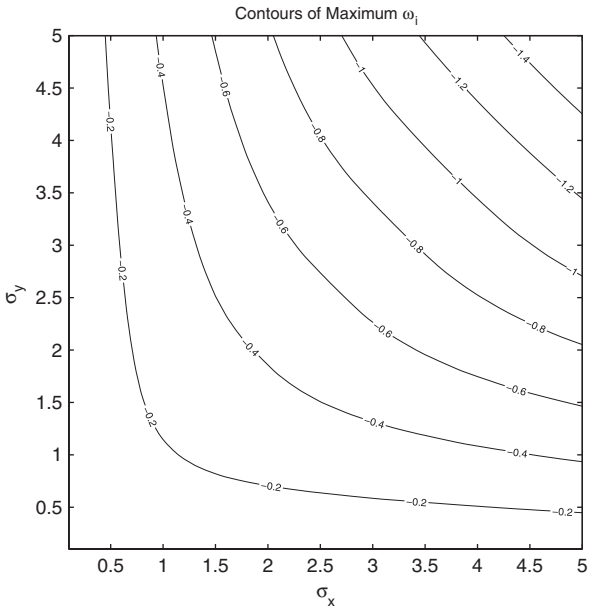

Figure 4. Contours of maximum imaginary part of ω for $M_x = M_y = 0.5$ and $|k_x|, |k_y| \leqslant 20$.

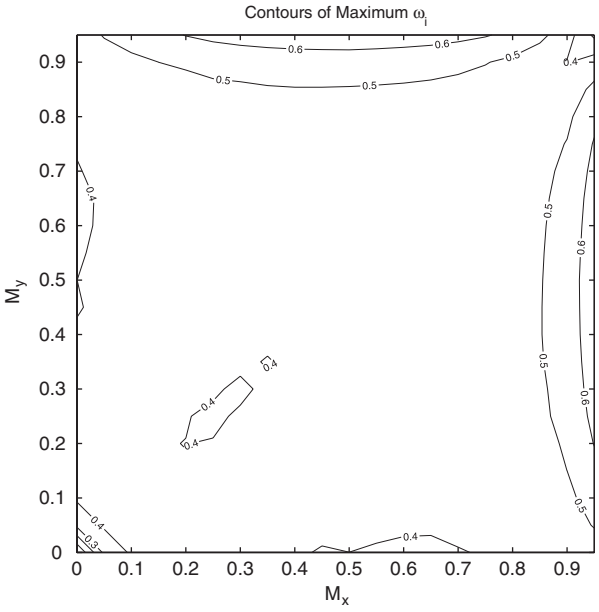

Figure 5. Existence of positive ω_i shows that the added terms are necessary for the stability of the corner equations.

Copyright © 2008 John Wiley & Sons, Ltd.

DOI: 10.1002/fld

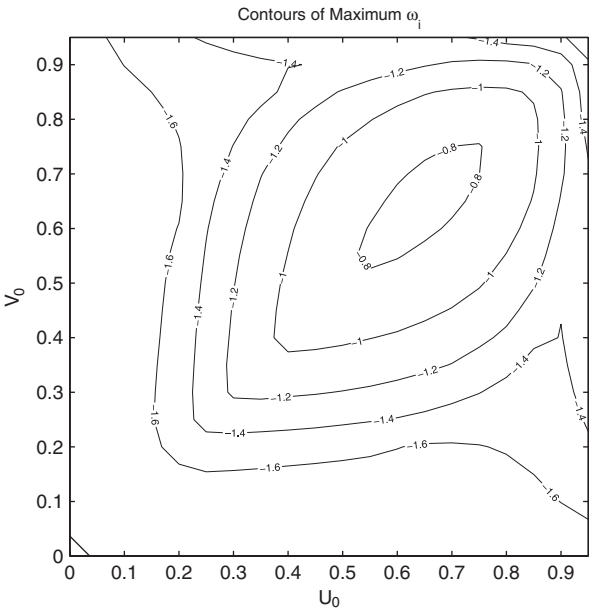

Figure 6. Contours of maximum imaginary part of ω for $\sigma_x = \sigma_y = 2.0$ and $|k_x|, |k_y| \leqslant 20$.

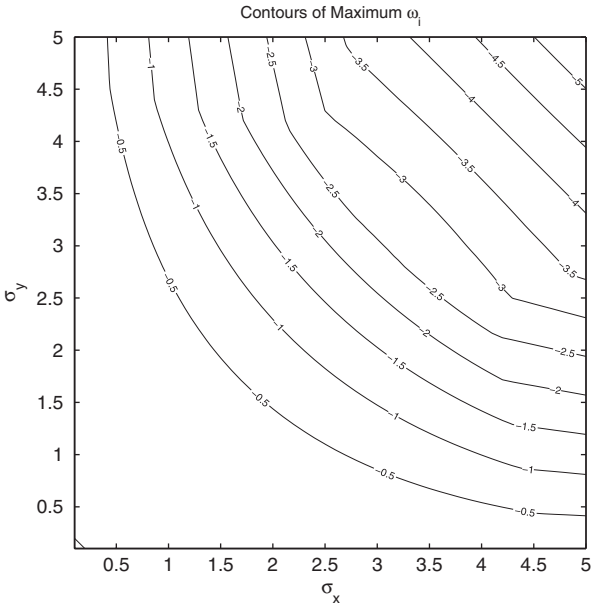

Figure 7. Contours of maximum imaginary part of ω for $U_0 = V_0 = 0.5$ and $|k_x|, |k_y| \leqslant 20$.

Copyright © 2008 John Wiley & Sons, Ltd.

DOI: 10.1002/fld

4. PML FOR THE NONLINEAR EULER EQUATIONS WITH OBLIQUE MEAN FLOW

We will use a similar approach in formulating PML equations for the nonlinear Euler equations, considering x- and y-layers individually, then constructing stable corner layers. For easy implementation, the Euler equations are kept in conservation form:

$$\frac{\partial \mathbf{u}}{\partial t}+\frac{\partial \mathbf{F}_1(\mathbf{u})}{\partial x}+\frac{\partial \mathbf{F}_2(\mathbf{u})}{\partial y}=0 \tag{16}$$

with

$$\mathbf{u}=\begin{pmatrix}\rho\\ \rho u\\ \rho v\\ \rho e\end{pmatrix},\quad \mathbf{F}_1(\mathbf{u})=\begin{pmatrix}\rho u\\ \rho u^2+p\\ \rho uv\\ \rho hu\end{pmatrix},\quad \mathbf{F}_2(\mathbf{u})=\begin{pmatrix}\rho v\\ \rho uv\\ \rho v^2+p\\ \rho hv\end{pmatrix} \tag{17}$$

and

$$h=e+\frac{p}{\rho},\quad p=(\gamma-1)\rho\left(e-\frac{u^2+v^2}{2}\right) \tag{18}$$

where ρ is the density, u and v are components of velocity, p is the pressure, and e is the energy. We also assume that an oblique background flow is moving with a constant velocity (U_0, V_0). The velocities are nondimensionalized by the speed of sound.

We can improve efficiency by designing the PML to absorb only the fluctuating part of $\mathbf{u}$, which is often smaller in amplitude than the total variable itself. Therefore, we begin by partitioning the solution inside the PML domain into two parts as follows:

$$\mathbf{u}=\bar{\mathbf{u}}+\mathbf{u}' \tag{19}$$

where $\mathbf{u}'$ is the time-dependent perturbation, which we seek to absorb, and $\bar{\mathbf{u}}$ is the time-independent oblique background flow, which satisfies the steady Euler equations,

$$\frac{\partial \mathbf{F}_1(\bar{\mathbf{u}})}{\partial x}+\frac{\partial \mathbf{F}_2(\bar{\mathbf{u}})}{\partial y}=0 \tag{20}$$

The part $\bar{\mathbf{u}}$ is an approximation of the actual mean flow. A more thorough discussion of pseudo mean flow can be found in [13]. The part $\mathbf{u}'$ will then be the focus of our PML equations, as it is the part we seek to absorb. The equation for $\mathbf{u}'$ then becomes

$$\frac{\partial \mathbf{u}'}{\partial t}+\frac{\partial[\mathbf{F}_1-\bar{\mathbf{F}}_1]}{\partial x}+\frac{\partial[\mathbf{F}_2-\bar{\mathbf{F}}_2]}{\partial y}=0 \tag{21}$$

where the shorthand notations $\mathbf{F}_1=\mathbf{F}_1(\mathbf{u})$, $\bar{\mathbf{F}}_1=\mathbf{F}_1(\bar{\mathbf{u}})$, $\mathbf{F}_2=\mathbf{F}_2(\mathbf{u})$, and $\bar{\mathbf{F}}_2=\mathbf{F}_2(\bar{\mathbf{u}})$ have been used.

To construct the x-layer equations, we now introduce a moving-frame change of variables

$$\hat{x}=x \tag{22a}$$

$$\hat{y}=y-V_0t \tag{22b}$$

$$\hat{t}=t \tag{22c}$$

Copyright © 2008 John Wiley & Sons, Ltd.

DOI: 10.1002/fld

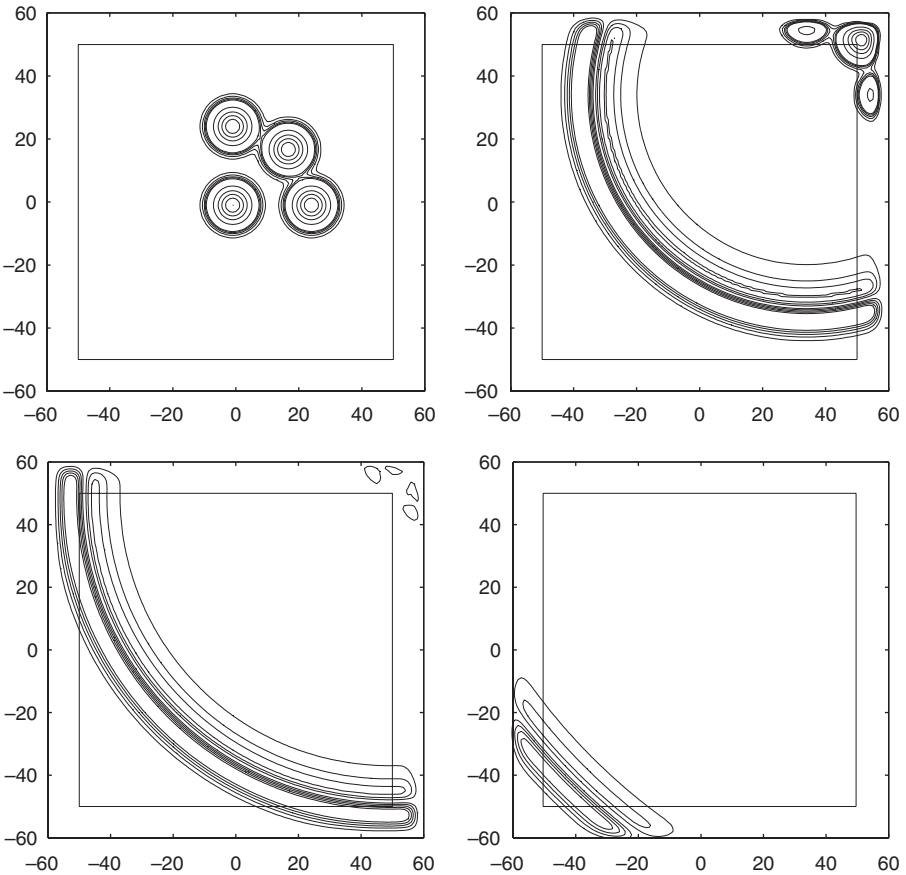

Figure 8. Contours of density at times $t=0$, 70, 100, and 200, plotted at levels 0.01:0.01:0.05, 0.2:0.2:1, $-0.1:-0.1:-1$, and $-0.01:-0.01:-0.05$, showing three entropy waves and an acoustic wave located at the center. The mean flow Mach numbers are $M_x=M_y=0.5$, and $D=10\Delta x$, $\alpha=3$.

that gives

$$\frac{\partial \mathbf{u}'}{\partial \hat{t}}+\frac{\partial[\mathbf{F}_1-\bar{\mathbf{F}}_1]}{\partial \hat{x}}+\frac{\partial[\mathbf{F}_2-\bar{\mathbf{F}}_2-V_0\mathbf{u}']}{\partial \hat{y}}=0 \tag{23}$$

In the moving-frame, the background flow in the vertical direction is stationary; hence, the PML equations are the same as those given in [13], which become

$$\frac{\partial \mathbf{u}'}{\partial \hat{t}}+\frac{\partial[\mathbf{F}_1-\bar{\mathbf{F}}_1]}{\partial \hat{x}}+\frac{\partial[\mathbf{F}_2-\bar{\mathbf{F}}_2-V_0\mathbf{u}']}{\partial \hat{y}}+\sigma_x\mathbf{q}_1+\sigma_x\beta_x[\mathbf{F}_1-\bar{\mathbf{F}}_1]=0 \tag{24a}$$

$$\frac{\partial \mathbf{q}_1}{\partial \hat{t}}+\frac{\partial[\mathbf{F}_1-\bar{\mathbf{F}}_1]}{\partial \hat{x}}+\sigma_x\mathbf{q}_1+\sigma_x\beta_x[\mathbf{F}_1-\bar{\mathbf{F}}_1]=0 \tag{24b}$$

Copyright © 2008 John Wiley & Sons, Ltd.

DOI: 10.1002/fld

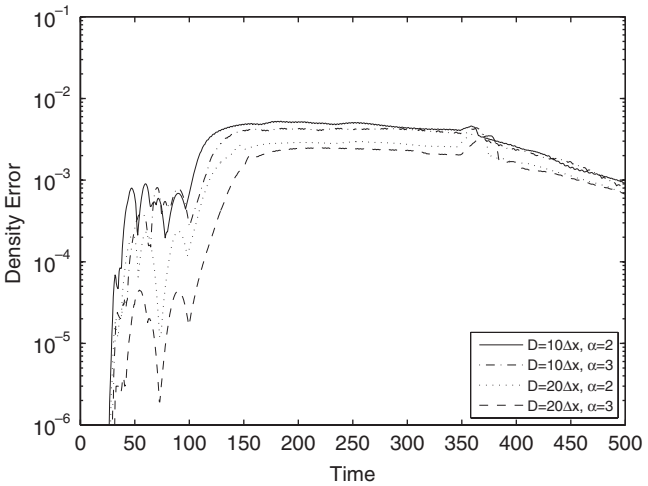

Figure 9. Maximum difference in density ρ between the numerical and reference solutions along $x=\pm 45$ and $y=\pm 45$ for varying PML width D and absorption coefficient parameter α.

where

$$\beta_x = \frac{U_0}{1-U_0^2} \tag{25}$$

Because we are dealing only with the x-layers, σ_y has been set to zero. Reverting back to the original time and space coordinates, we arrive at the nonlinear x-layer equations:

$$\frac{\partial \mathbf{u}}{\partial t} + \frac{\partial[\mathbf{F}_1 - \bar{\mathbf{F}}_1]}{\partial x} + \frac{\partial[\mathbf{F}_2 - \bar{\mathbf{F}}_2]}{\partial y} + \sigma_x \mathbf{q}_1 + \sigma_x \beta_x [\mathbf{F}_1 - \bar{\mathbf{F}}_1] = 0 \tag{26a}$$

$$\frac{\partial \mathbf{q}_1}{\partial t} + \frac{\partial[\mathbf{F}_1 - \bar{\mathbf{F}}_1]}{\partial x} + V_0 \frac{\partial \mathbf{q}_1}{\partial y} + \sigma_x \mathbf{q}_1 + \sigma_x \beta_x [\mathbf{F}_1 - \bar{\mathbf{F}}_1] = 0 \tag{26b}$$

A similar derivation leads to the y-layer equations:

$$\frac{\partial \mathbf{u}}{\partial t} + \frac{\partial[\mathbf{F}_1 - \bar{\mathbf{F}}_1]}{\partial x} + \frac{\partial[\mathbf{F}_2 - \bar{\mathbf{F}}_2]}{\partial y} + \sigma_y \mathbf{q}_2 + \sigma_y \beta_y [\mathbf{F}_2 - \bar{\mathbf{F}}_2] = 0 \tag{27a}$$

$$\frac{\partial \mathbf{q}_2}{\partial t} + U_0 \frac{\partial \mathbf{q}_2}{\partial x} + \frac{\partial[\mathbf{F}_2 - \bar{\mathbf{F}}_2]}{\partial y} + \sigma_y \mathbf{q}_2 + \sigma_y \beta_y [\mathbf{F}_2 - \bar{\mathbf{F}}_2] = 0 \tag{27b}$$

where

$$\beta_y = \frac{V_0}{1-V_0^2} \tag{28}$$

Copyright © 2008 John Wiley & Sons, Ltd.

DOI: 10.1002/fld

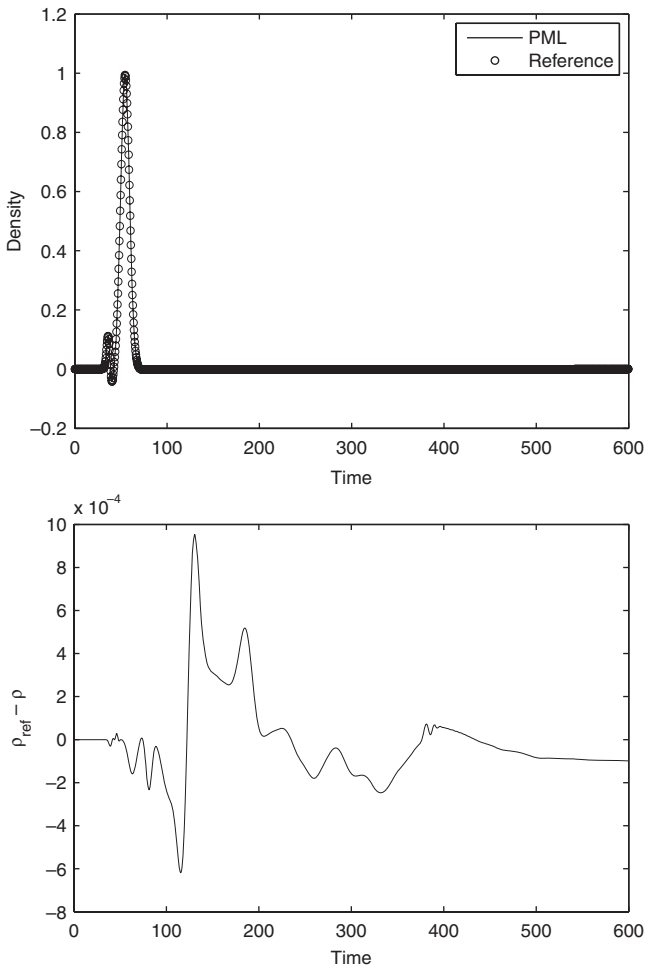

Figure 10. Top figure plots PML and reference solutions of density at the point (45, 45) as a function of time. Bottom figure plots the difference between the two solutions at the same point as a function of time.

and σ_x has been set to zero. Again, corner layers will be constructed by combining Equation sets (26) and (27):

$$\frac{\partial \mathbf{u}}{\partial t}+\frac{\partial[\mathbf{F}_1-\bar{\mathbf{F}}_1]}{\partial x}+\frac{\partial[\mathbf{F}_2-\bar{\mathbf{F}}_2]}{\partial y}+\sigma_x\mathbf{q}_1+\sigma_y\mathbf{q}_2+\sigma_x\beta_x[\mathbf{F}_1-\bar{\mathbf{F}}_1]+\sigma_y\beta_y[\mathbf{F}_2-\bar{\mathbf{F}}_2]+\sigma_x\sigma_y(\mathbf{u}-\bar{\mathbf{u}})=0 \tag{29a}$$

$$\frac{\partial \mathbf{q}_1}{\partial t}+\frac{\partial[\mathbf{F}_1-\bar{\mathbf{F}}_1]}{\partial x}+V_0\frac{\partial \mathbf{q}_1}{\partial y}+(\sigma_x+\sigma_y)\mathbf{q}_1+\sigma_x\beta_x[\mathbf{F}_1-\bar{\mathbf{F}}_1]=0 \tag{29b}$$

Copyright © 2008 John Wiley & Sons, Ltd.

DOI: 10.1002/fld

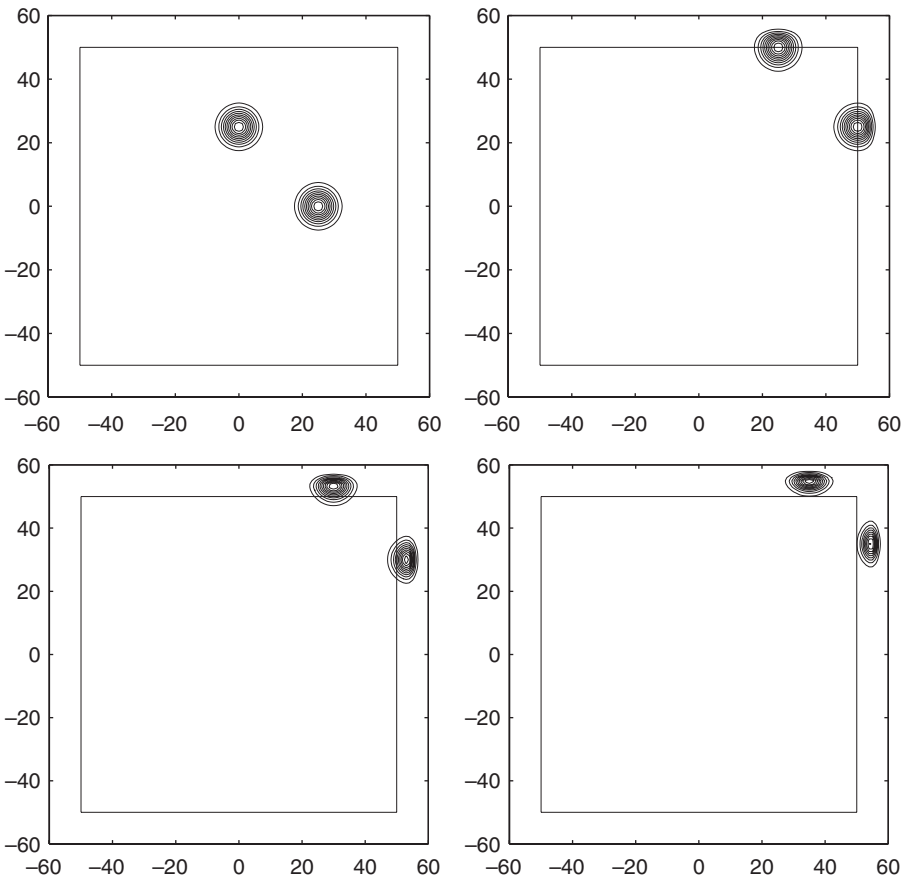

Figure 11. Contours of density at times $t=0$, 50, 60, and 70, plotted at levels 0.01:0.01:0.05, 0.05:0.05:1, $-0.1:-0.1:-1$, and $-0.01:-0.02:-0.05$. The mean flow Mach numbers are $M_x=M_y=0.5$, and $D=10\Delta x$, $\alpha=3$.

$$\frac{\partial \mathbf{q}_2}{\partial t}+U_0\frac{\partial \mathbf{q}_2}{\partial x}+\frac{\partial[\mathbf{F}_2-\bar{\mathbf{F}}_2]}{\partial y}+(\sigma_x+\sigma_y)\mathbf{q}_2+\sigma_y\beta_y[\mathbf{F}_2-\bar{\mathbf{F}}_2]=0 \tag{29c}$$

For stability, the terms $\sigma_x\sigma_y(\mathbf{u}-\bar{\mathbf{u}})$, $\sigma_y\mathbf{q}_1$, and $\sigma_x\mathbf{q}_2$ have been added to Equations (29a), (29b), and (29c), respectively. These additional terms are chosen so that they vanish within the side layers. That is, when σ_y or σ_x is zero, Equation set (29) reduces to the x- or y-layer equation sets, (26) or (27), respectively. Although there are other choices of additional terms that would also disappear in the side layers, the current choice will make the layer stable, as will be shown below. The following section presents the details of the stability analysis for the corner equations presented in Sections 3 and 4.

Copyright © 2008 John Wiley & Sons, Ltd.

DOI: 10.1002/fld

5. STABILITY ANALYSIS OF CORNER EQUATIONS

We will first present the linear stability analysis of the corner layer equations given in (15). Stability is tested by substituting

$$\begin{pmatrix} \mathbf{u} \\ \mathbf{q}_1 \\ \mathbf{q}_2 \end{pmatrix} = \mathrm{e}^{\mathrm{i}(k_x x + k_y y - \omega t)} \begin{pmatrix} \hat{\mathbf{u}} \\ \hat{\mathbf{q}}_1 \\ \hat{\mathbf{q}}_2 \end{pmatrix} \tag{30}$$

into these linearized equations, which forms an eigenvalue problem for $\hat{\mathbf{u}}$, $\hat{\mathbf{q}}_1$, and $\hat{\mathbf{q}}_2$. Assuming σ_x and σ_y to be constants, solutions for the resulting eigenvalue equation for ω are checked for positive imaginary parts for given values of k_x and k_y. If none of the eigenvalues has a positive imaginary part, the system is known to be dynamically stable. Figure 3 shows the contours of the maximum value of ω_i, the imaginary part of ω, for subsonic values of M_x and M_y over the range $0 \leqslant M_x, M_y \leqslant 0.95$, given wavenumbers $|k_x|, |k_y| \leqslant 20$. In this case, all values of ω_i are found to be negative, indicating a stable system. Alternatively, M_x and M_y can be held constant, and contours of maximum ω_i values for $0 \leqslant \sigma_x, \sigma_y \leqslant 5$, $|k_x|, |k_y| \leqslant 20$ can be plotted, as is done in Figure 4. Again, all maximum imaginary eigenvalues are found to be negative, indicating that the proposed equations are stable. To show the necessity of the terms $\sigma_y \mathbf{q}_1$ and $\sigma_x \mathbf{q}_2$ that have been added to Equations (15b) and (15c), respectively, Figure 5 plots the maximum ω_i over subsonic Mach numbers M_x and M_y for $\sigma_x = \sigma_y = 2.0$ for equations equivalent to those given in (15) but with the additional terms omitted. The existence of positive ω_i indicates that these terms are required to maintain the stability of the corner equations.

A similar approach has been used to analyze the linear stability of the PML for the nonlinear Euler equations, given in (29) and linearized around the background mean flow. Figures 6 and 7 show the results of such an analysis. Nonpositive maximum ω_i again indicates that the proposed system is stable.

6. NUMERICAL EXAMPLES

6.1. Acoustic, vorticity, and entropy waves

We evaluate the effectiveness of a PML of width D for the linearized Euler equations by testing the PML with acoustic, vorticity, and entropy waves traveling with mean flow $(M_x, M_y) = (0.5, 0.5)$ in the domain $[-50, 50] \times [-50, 50]$, discretized by $\Delta x = \Delta y = 1$. Four initial waves are given as

$$\rho = \mathrm{e}^{-(\ln 2)\frac{x^2+y^2}{16}} + \sum_{n=1}^{3} \mathrm{e}^{-(\ln 2)\frac{(x-x_n)^2+(y-y_n)^2}{16}} \tag{31a}$$

$$u = \sum_{n=1}^{3} (y - y_n) \mathrm{e}^{-(\ln 2)\frac{(x-x_n)^2+(y-y_n)^2}{16}} \tag{31b}$$

$$v = -\sum_{n=1}^{3} (x - x_n) \mathrm{e}^{-(\ln 2)\frac{(x-x_n)^2+(y-y_n)^2}{16}} \tag{31c}$$

$$p = \mathrm{e}^{-(\ln 2)\frac{x^2+y^2}{16}} \tag{31d}$$

Copyright © 2008 John Wiley & Sons, Ltd.

DOI: 10.1002/fld

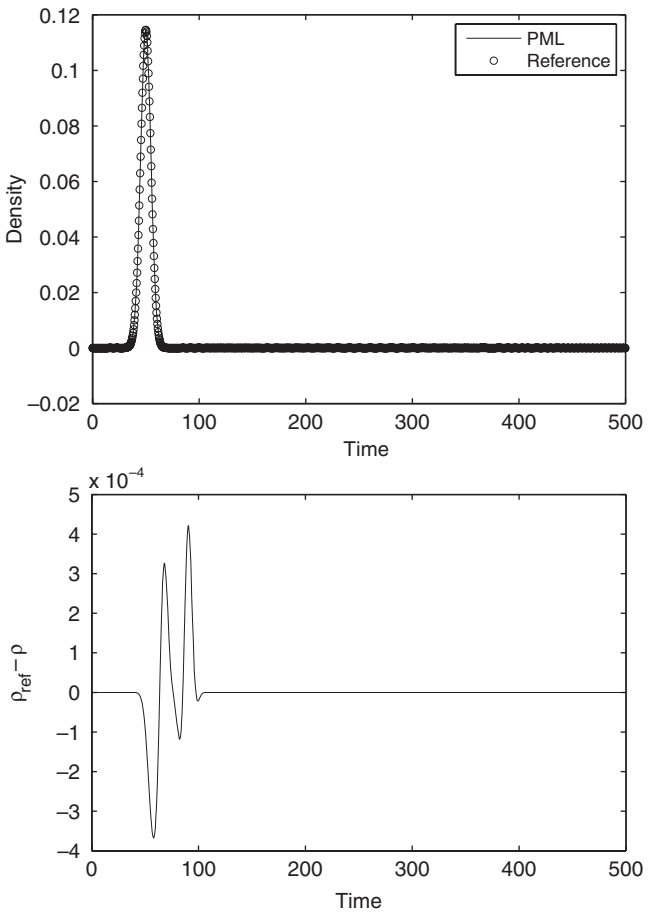

Figure 12. Top figure plots PML and reference solutions of density at the point $(45, 30)$ as a function of time. Bottom figure plots the difference between the two solutions at the same point as a function of time.

where ρ is the density, u and v are the x- and y-components of velocity, respectively, and p is the pressure. The initial condition represents an acoustic pulse at $(x, y) = (0, 0)$ and entropy and vorticity pulses at $(x_1, y_1) = (25, 0)$, $(x_2, y_2) = \frac{\sqrt{2}}{2}(25, 25)$, and $(x_3, y_3) = (0, 25)$. In particular, the vorticity and entropy waves will be convected toward the upper-right corner of the computational domain.

The linearized Euler equation (1) is solved in the physical domain and Equations (15) are solved in the added PML absorbing domains, as shown in Figure 8. The absorption coefficient σ_x is defined

$$\sigma_x = \sigma_{\max} \left| \frac{x - x_0}{D} \right|^{\alpha} \tag{32}$$

Copyright © 2008 John Wiley & Sons, Ltd.

DOI: 10.1002/fld

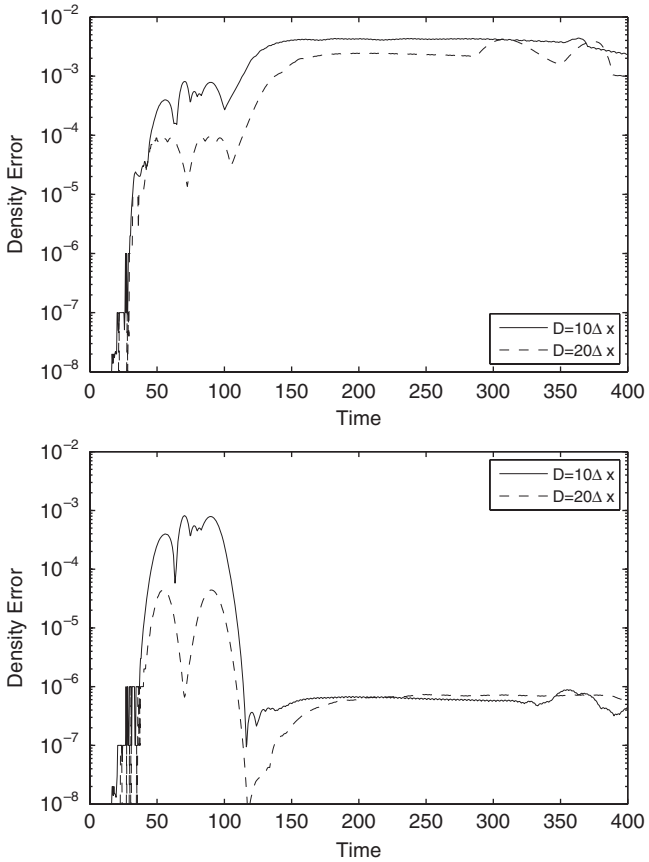

Figure 13. Maximum differences in density ρ between the numerical and reference solutions along $x = \pm 45$ and $y = \pm 45$ for varying PML widths, comparing the case where waves exit out of the side and corner layers (top) with the case where waves exit out of the side layer only (bottom).

where x_0 is the location of the interface between the Euler and PML domains. In this example, $x_0 = \pm 50$ for the PML at the right and the left boundaries, respectively. The coefficient σ_y is similarly defined. Figure 8 shows the contours of density at times $t = 0, 70, 100,$ and 200 for a PML of width $D = 10\Delta x = 10\Delta y$ and absorption coefficient parameters $\sigma_{\max} = 2$ and $\alpha = 3$. The waves appear to exit the domain with little reflection.

For a more quantitative evaluation, solutions along $x = \pm 45$ and $y = \pm 45$ are compared with those from calculations on the larger domain $[-400, 400] \times [-400, 400]$. Figure 9 plots as a function of time the magnitude of the maximum difference between the two solutions for density along the selected comparison points for varying values of D and α. This is equivalent to the reflection coefficient for density, as the maximum amplitude is one. As the width of the PML increases, there is a noticeable decrease in the reflection error. In particular, an increase in the PML width has a significant effect on the reduction of reflection error before $t = 100$, when the vortices are absorbed by the side layers. The reflection errors are seen increased when the vorticity and the

Copyright © 2008 John Wiley & Sons, Ltd.

DOI: 10.1002/fld

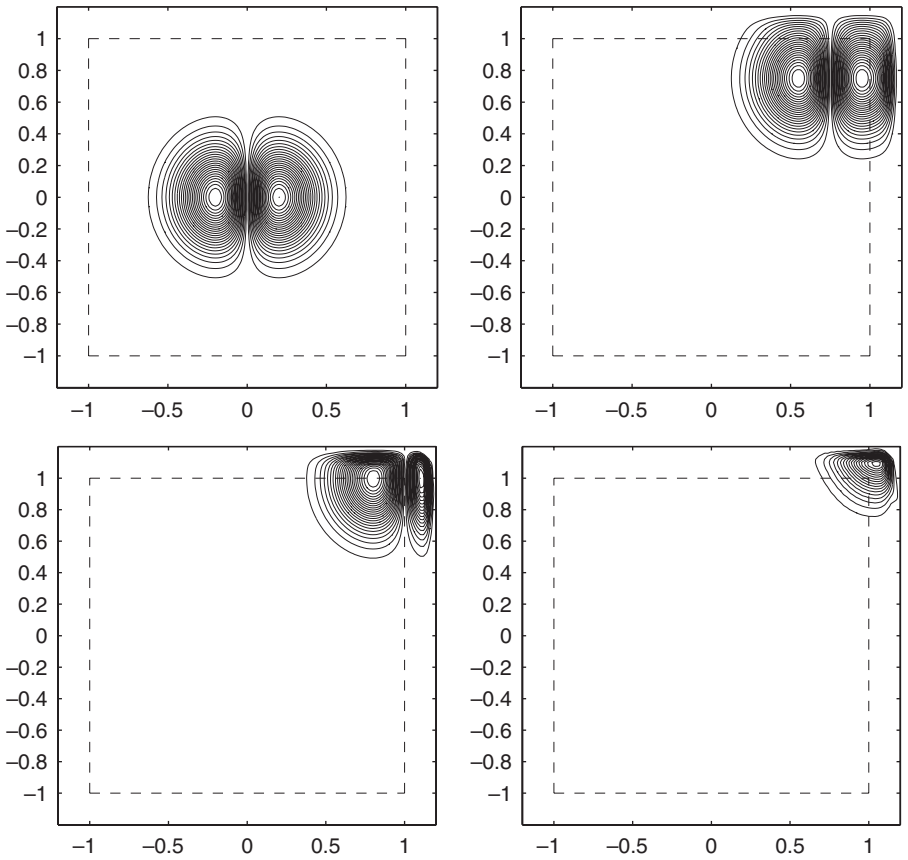

Figure 14. Contours of v-velocity at times $t = 0, 1.5, 2.0, 2.5$.

entropy pulses enter the corner layer, and the increase in the PML width has a smaller effect on the reduction of reflection error. This confirms that the interfaces between the Euler domain and the side layers are perfectly matched, whereas those between the corner and sides layers are not. Despite this, reflection errors on the whole remain small for the duration of the tested time. For further comparison, the top plot of Figure 10 shows the time history of density at the point $(45, 45)$ for both the numerical and reference solutions. The solutions appear to be in very good agreement. The bottom plot of Figure 10 is the difference between the numerical and reference solutions at the same point as a function of time. The magnitude of this difference is smaller than 10^{-3}.

6.2. Vorticity and entropy waves at side layers

To see the effects of the unmatched corner layers on the accuracy, we modify the previous example so that no waves exit out of the corner region. This is done by omitting the initial acoustic wave

Copyright © 2008 John Wiley & Sons, Ltd.

DOI: 10.1002/fld

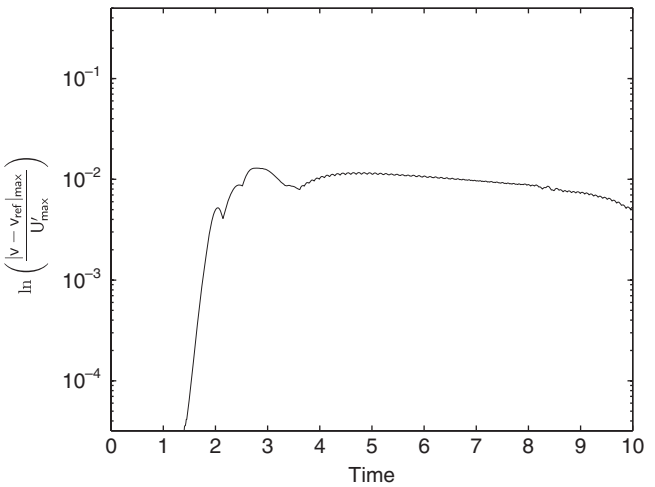

Figure 15. Reflection coefficient versus time for v-velocity along $x = \pm 0.9$ and $y = \pm 0.9$ for $U_0 = V_0 = 0.5$ and $U'_{\max} = 0.25$.

that was initialized at $(0, 0)$ and the vorticity and entropy waves that were initialized at the point $(x_2, y_2) = \frac{\sqrt{2}}{2}(25, 25)$. The initial condition is therefore given as

$$\rho = \mathrm{e}^{-(\ln 2)\frac{(x-25)^2+y^2}{16}} + \mathrm{e}^{-(\ln 2)\frac{x^2+(y-25)^2}{16}} \tag{33a}$$

$$u = y\mathrm{e}^{-(\ln 2)\frac{(x-25)^2+y^2}{16}} + (y-25)\mathrm{e}^{-(\ln 2)\frac{x^2+(y-25)^2}{16}} \tag{33b}$$

$$v = -(x-25)\mathrm{e}^{-(\ln 2)\frac{(x-25)^2+y^2}{16}} - x\mathrm{e}^{-(\ln 2)\frac{x^2+(y-25)^2}{16}} \tag{33c}$$

$$p = 0 \tag{33d}$$

The remainder of the configuration is identical to the previous example. Figure 11 shows the contours of density at times $t = 0, 50, 60$, and 70.

To assess the accuracy, the solution of density at the point $(45, 30)$ is plotted against the larger domain reference solution as a function of time in the top plot of Figure 12. The bottom plot shows the difference between the two solutions at that same point. For this pointwise comparison, the results are comparable to those of the previous example, with the order of magnitude for the pointwise difference at around 10^{-3}. The maximum difference error for density along the points $x = \pm 45$ and $y = \pm 45$ is plotted in Figure 13 for varying PML widths. With no waves exiting out of the corner, there is a noticeable decrease in the maximum difference.

Copyright © 2008 John Wiley & Sons, Ltd.

DOI: 10.1002/fld

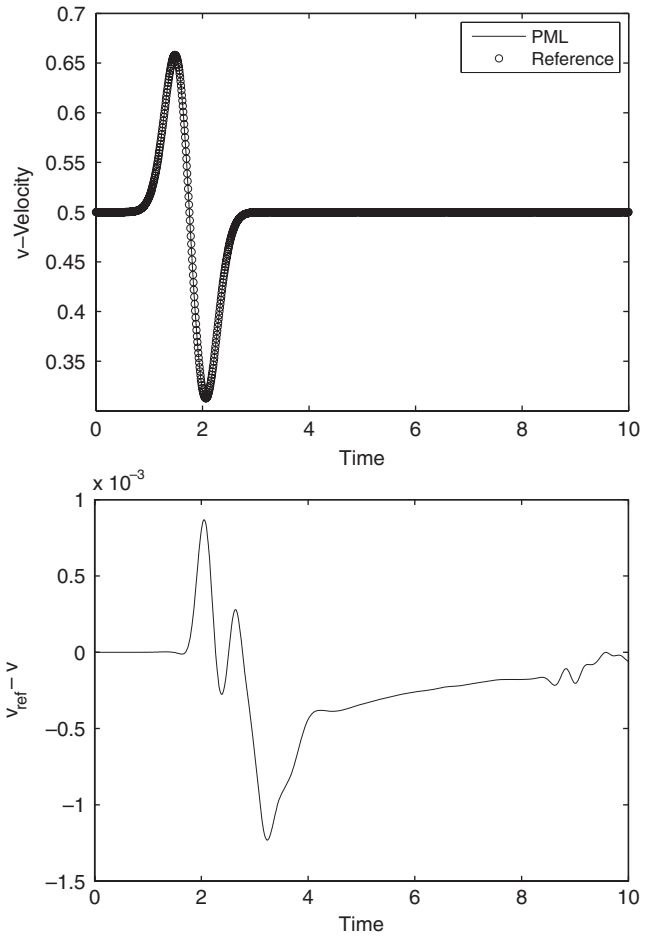

Figure 16. Top figure plots PML and reference solutions of v-velocity at the point $(0.9, 0.9)$ as a function of time. Bottom figure plots the difference between the two solutions at the same point as a function of time.

6.3. Isentropic vortex

We will test the nonlinear PML equations for an exact solution of the nonlinear Euler equations, a convecting vortex of the form

$$\begin{pmatrix} \rho(\mathbf{x},t) \\ u(\mathbf{x},t) \\ v(\mathbf{x},t) \\ p(\mathbf{x},t) \end{pmatrix} = \begin{pmatrix} 0 \\ U_0 \\ V_0 \\ 0 \end{pmatrix} + \begin{pmatrix} \rho_r(r) \\ -u_r(r)\sin\theta \\ u_r(r)\cos\theta \\ p_r(r) \end{pmatrix} \tag{34}$$

Copyright © 2008 John Wiley & Sons, Ltd.

DOI: 10.1002/fld

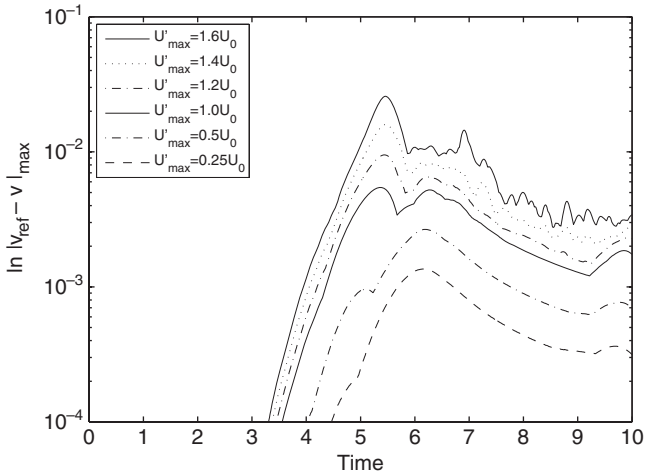

Figure 17. Maximum difference versus time for v-velocity along $x = \pm 0.9$ and $y = \pm 0.9$ for $U_0 = V_0 = 0.2$ and varying $U'_{\max}$.

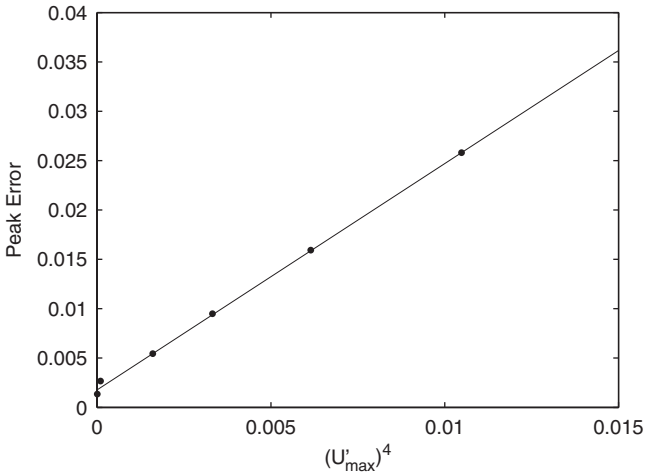

Figure 18. Relationship between peak difference errors and maximum wave amplitude $U'_{\max}$.

where $r = \sqrt{(x - U_0 t)^2 + (y - V_0 t)^2}$, and for a given $u_r(r)$ and $\rho_r(r)$, the pressure $p_r(r)$ is given as

$$\frac{\mathrm{d}}{\mathrm{d}r} p_r(r) = \rho_r(r) \frac{u_r^2(r)}{r} \tag{35}$$

This solution to the nonlinear Euler equations advects with the constant velocity (U_0, V_0). For this example, we will assume a velocity distribution of the form

$$u_r(r) = \frac{U'_{\max}}{b} r \mathrm{e}^{(1/2)(1 - r^2/b^2)} \tag{36}$$

Copyright © 2008 John Wiley & Sons, Ltd.

DOI: 10.1002/fld

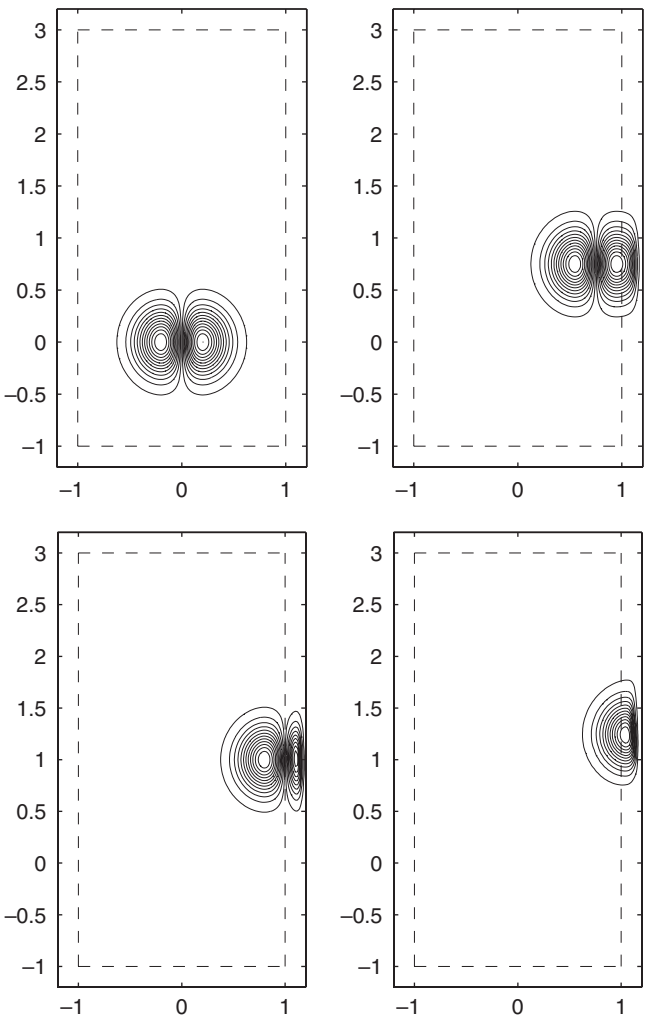

Figure 19. Contours of v-velocity at times $t=0, 1.5, 2.0, 2.5$.

where $U'_{\max}$ is the maximum velocity of $u_r(r)$ at $r=b$. For isentropic flow, we enforce the relationship

$$p_r = \frac{1}{\gamma}\rho_r^{\gamma} \tag{37}$$

that leads to the following density and pressure distributions:

$$\rho_r(r) = (1-\tfrac{1}{2}(\gamma-1)U'^2_{\max}\mathrm{e}^{1-r^2/b^2})^{1/(\gamma-1)} \tag{38}$$

$$p_r(r) = \frac{1}{\gamma}(1-\tfrac{1}{2}(\gamma-1)U'^2_{\max}\mathrm{e}^{1-r^2/b^2})^{\gamma/(\gamma-1)} \tag{39}$$

Copyright © 2008 John Wiley & Sons, Ltd.

DOI: 10.1002/fld

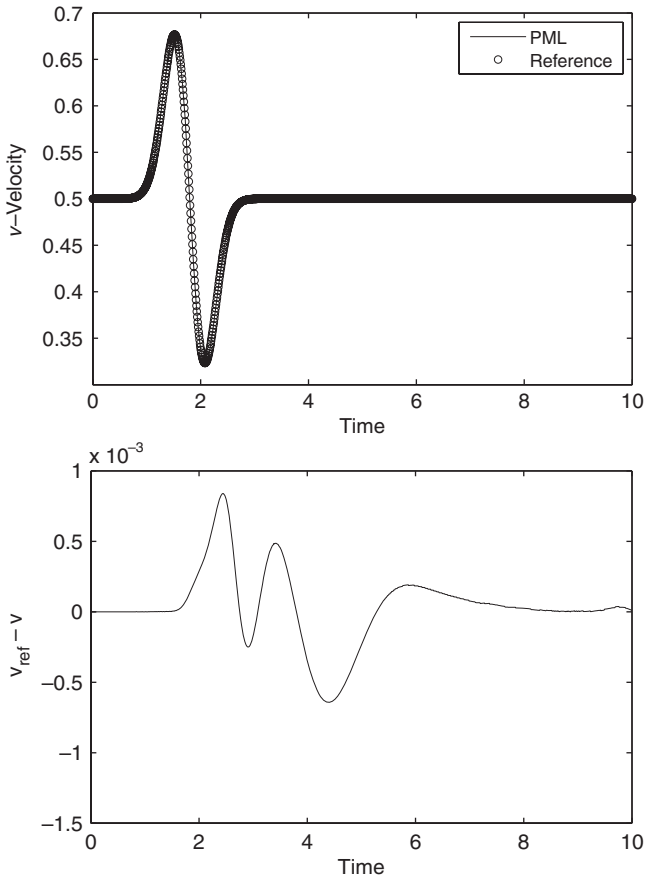

Figure 20. Top figure plots PML and reference solutions of v-velocity at the point $(0.9, 0.9)$ as a function of time. Bottom figure plots the difference between the two solutions at the same point as a function of time.

Figure 14 shows the contours of v-velocity at $t=0$, 1.5, 2.0, and 2.5. Constant background velocity was taken to be $(U_0, V_0)=(0.5, 0.5)$, and in the above distributions, $U'_{\max}=0.25$, $b=0.2$, and $\gamma=1.4$. The PML width was chosen to be 10 grid points, and the entire domain $[-1.2, 1.2]\times[-1.2, 1.2]$ was discretized by $\Delta x=\Delta y=0.02$. For the PML absorption coefficients, σ_x and σ_y, parameter values $\sigma_{\max}=20$ and $\alpha=4$ were chosen in the form (32). To test the accuracy, numerical solutions were compared with the reference solutions computed on the larger domain $[-6.2, 6.2]\times[-6.2, 6.2]$. The reflection coefficient for v-velocity is calculated as the maximum difference between the numerical and reference solutions along $x=\pm 0.9$ and $y=\pm 0.9$ normalized by the maximum amplitude $U'_{\max}$ and is plotted in Figure 15 as a function of time. The top plot of Figure 16 plots the time history of the v-velocity component of the numerical and reference solutions at the point $(0.9, 0.9)$. Very good agreement is seen between the two solutions. The bottom plot of Figure 16 is the difference between the numerical and reference solutions at the same point as a function of time. The magnitude of the difference is approximately 10^{-3}.

Copyright © 2008 John Wiley & Sons, Ltd.

DOI: 10.1002/fld

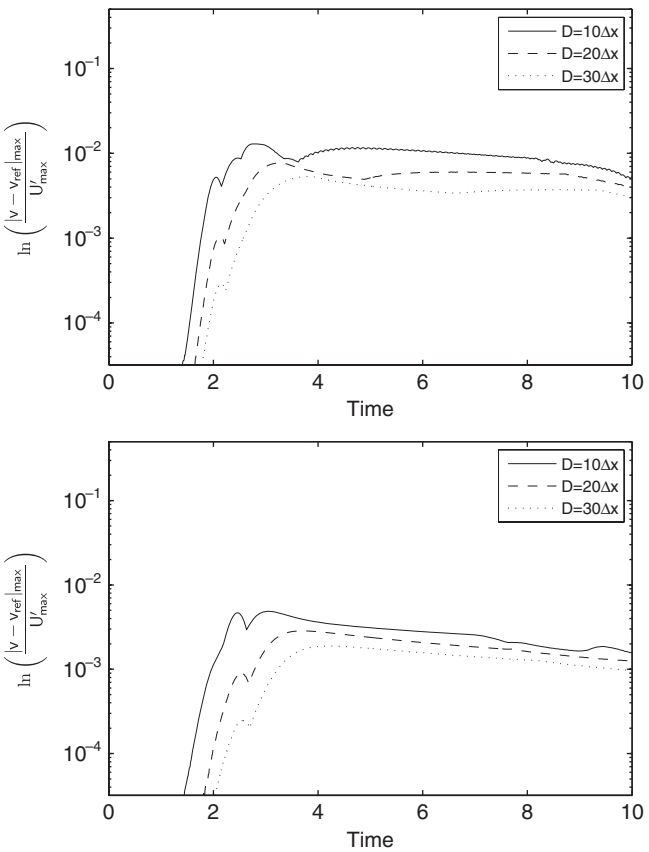

Figure 21. Reflection coefficients versus time for v-velocity along $x=\pm 0.9$ and $y=\pm 0.9$ for $U_0=V_0=0.5$, $U'_{\max}=0.25$, and varying PML widths. Differences are compared for waves exiting through either the corner layer (top) or the side layer (bottom).

Satisfactory results were also achieved for various cases of higher strength vortices. Taking $(U_0, V_0)=(0.2, 0.2)$, vortex strengths $U'_{\max}=1.0U_0, 1.2U_0, 1.4U_0, 1.6U_0$ were tested. The maximum difference between the numerical and large domain calculations is plotted in Figure 17 for each case. For comparison, the errors for the cases of weaker vortices, $U'_{\max}=0.25U_0, 0.5U_0$ are also plotted. In general, the difference increases with the strength of the vortex. Note that when $U'_{\max}>U_0$, part of the vortex has a velocity opposite to the uniform background flow. When $U'_{\max}$ is relatively small compared to U_0, error levels are close to those of linearized cases. The peak errors appear to scale with the fourth power of the amplitude, which is shown in Figure 18.

The accuracy of the calculation for the vortex exiting through the unmatched corner layer is again compared with the accuracy of a calculation where the vortex exits out of the side layer only. This side layer calculation is carried out by extending the domain in the positive y-direction, so that the new domain is $[-1.2, 1.2]\times[-1.2, 3.2]$. Contour plots are given for v-velocity in Figure 19, where again there is no visible reflection. In the pointwise comparisons given in Figure 20, a

Copyright © 2008 John Wiley & Sons, Ltd.

DOI: 10.1002/fld

small decrease in the magnitude of the difference error is seen in comparison with the previous calculation. Finally, in Figure 21, the reflection coefficients for v-velocity for this and the previous calculation are compared for varying PML widths. In both cases, an increase in the PML width does not result in as significant a decrease in reflection errors as that observed in the case of the matched linear side layer in Figure 13. This is expected as the PML method does not result in perfect matching for the nonlinear case.

7. CONCLUSIONS

PML absorbing boundary conditions for the linearized and the nonlinear Euler equations have been derived in the form of x-, y-, and corner layer equations for the case of mean flow in an arbitrary direction. The x- and y-layer equations are perfectly matched for linear waves, whereas the corner layer equations were shown to be stable. The proposed equations performed well in the given examples.

The capability of PML equations to absorb the outgoing waves traveling with an oblique mean flow is an important step in the movement toward modeling effective nonreflecting boundary conditions for increasingly realistic aeroacoustic problems. Such capability will allow for a number of new configurations to be tested numerically.

ACKNOWLEDGEMENTS

This work is supported by a grant from the National Science Foundation DMS-0411402.

REFERENCES

1. Bérenger JP. A perfectly matched layer for the absorption of electromagnetic waves. *Journal of Computational Physics* 1994; **114**(2):185–200.
2. Bécache E, Dhia ASBB, Legendre G. Perfectly matched layers for the convected Helmholtz equation. *SIAM Journal on Numerical Analysis* 2004; **42**(1):409–433.
3. Bécache E, Fauqueux S, Joly P. Stability of perfectly matched layers, group velocities and anisotropic waves. *Journal of Computational Physics* 2003; **188**(2):399–433.
4. Hagstrom T, Nazarov I. Absorbing layers and radiation boundary conditions for jet flow simulations. *AIAA Paper 2002-2606*, 2002.
5. Hagstrom T, Nazarov I. Absorbing layers and radiation boundary conditions for shear flow calculations. *AIAA Paper 2003-3298*, 2003.
6. Hu FQ. On absorbing boundary conditions for linearized Euler equations by a perfectly matched layer. *Journal of Computational Physics* 1996; **129**(1):201–219.
7. Hu FQ. A stable perfectly matched layer for linearized Euler equations in unsplit physical variables. *Journal of Computational Physics* 2001; **173**(2):455–480.
8. Appelö D, Hagstrom T, Kreiss G. Perfectly matched layers for hyperbolic systems: general formulation, well-posedness and stability. *SIAM Journal on Applied Mathematics* 2006; **67**(1):1–23.
9. Diaz J, Joly P. A time domain analysis of PML models in acoustics. *Computer Methods in Applied Mechanics and Engineering* 2006; **195**(29–32):3820–3853.
10. Nataf F. A new approach to perfectly matched layers for the linearized Euler system. *Journal of Computational Physics* 2006; **214**(2):757–772.

Copyright © 2008 John Wiley & Sons, Ltd.

DOI: 10.1002/fld

11. Hu FQ. A perfectly matched layer absorbing boundary condition for linearized Euler equations with a non-uniform mean flow. *Journal of Computational Physics* 2005; **208**(2):469–492.
12. Hu FQ. On the construction of PML absorbing boundary condition for the non-linear Euler equations. *AIAA Paper 2006-0798*, 2006.
13. Hu FQ, Li XD, Lin DK. Absorbing boundary conditions for nonlinear Euler and Navier–Stokes equations based on the perfectly matched layer technique. *Journal of Computational Physics* 2008; **227**(9):4398–4424.

Copyright © 2008 John Wiley & Sons, Ltd.

DOI: 10.1002/fld